Journal of Materials Chemistry C

ROYAL SOCIETY OF CHEMISTRY

PAPER

View Article Online
View Journal

Cite this: DOI: 10.1039/d5tc02658j

Solid additive-enhanced performance in near-infrared organic photodetectors for broadband–narrowband dual-mode detection

Yu-Ching Huang, *[abc] Zhi-Hao Huang,[ac] Bo-Chen Chen,[a] Hou-Chin Cha[bd] and Kun-Mu Lee *[c]

Organic photodetectors (OPDs) are essential for applications in environmental monitoring, medical diagnostics, and telecommunications, particularly for detecting infrared to near-infrared (NIR) light. However, improving the detectivity of OPDs in these regions remains challenging due to the presence of high dark current and limited responsivity. In this study, we present the first use of a solid additive, ferrocene (Fc), in the active layer of PTB7-Th:BT-CIC to enhance its performance. This approach significantly reduced the dark current density to 6.81 × 10^{-9} A cm^{-2} and improved the responsivity to 0.45 A W^{-1} at 800 nm, with an external quantum efficiency (EQE) of 70%. Compared with 1-chloronaphthalene (CN), a commonly used liquid additive, Fc provided superior improvements in both electrical and optical properties as well as enhanced the molecular arrangement and carrier transport. Additionally, Fc optimization reduced the root-mean-square white noise ($I_{n,rms}$) to a minimum of 1.92 × 10^{-14} A with a specific detectivity (D^*_n) of 2.54 × 10^{12} Jones. Furthermore, we integrated an input optical filtering (IOF) perovskite filter into the OPD system, enabling narrowband NIR detection with an EQE of 43.9%, a responsivity of 0.294 A W^{-1} at 830 nm, and a full width at half maximum (FWHM) of 84.6. We also realized broadband–narrowband dual-mode NIR OPDs by introducing a transparent electrode under bidirectional illumination. Our study highlights the pioneering use of solid additives to optimize the performance of NIR OPDs while showcasing advanced detection capabilities by integrating perovskite filters and transparent electrodes.

Received 14th July 2025,
Accepted 6th August 2025

DOI: 10.1039/d5tc02658j

rsc.li/materials-c

1. Introduction

Organic photodetectors (OPDs) have attracted broad attention in diverse fields such as environmental monitoring, image sensing, optical communication, and biomedical applications because of their cost-effectiveness in manufacturing, solution processability, mechanical flexibility, broad absorption region, and tunable energy bandgap.[1] For infrared to near-infrared (NIR) detection, the response range of OPDs can be extended beyond 1000 nm by using low bandgap polymers or non-fullerene small molecules, offering superior spectral coverage compared to conventional Si-based photodetectors.[2] However, enhancing OPD performance in these regions remains challenging due to high dark current, which limits their practical application. Additionally, narrow-band detection with wavelength selectivity is a key feature in NIR detection applications. While conventional inorganic photodetectors, such as Si and III–V semiconductors, dominate the field of commercialized PDs due to their excellent detectivity and rapid response over a wide spectral region (400–1000 nm),[3] they require optical filters to achieve the goal of narrow-band detection. These optical filters are expensive, reduce the resolution, and have limited wavelength selectivity, making them less suitable for multicolor imaging and wearable devices. Furthermore, even after recent developments in hybrid organic–inorganic photodetectors, which attempted to modulate responses in both visible and NIR regions, they still suffer from a broad bandwidth (exceeding 100 nm) and low response (less than 0.1 A W^{-1}), limiting their effectiveness in narrowband detection in the NIR region. In contrast, OPDs can achieve excellent narrow-band detection by tailoring the donor and acceptor molecular structures to confine the absorption spectrum, thereby enabling a full width at half maximum (FWHM) response of ∼80 nm.[4] Recent efforts

[a] Department of Materials Engineering, and Biochemical Technology R&D Center, Ming Chi University of Technology, New Taipei City, 24301, Taiwan. E-mail: huangyc@mail.mcut.edu.tw
[b] Organic Electronics Research Center, Ming Chi University of Technology, New Taipei City 24301, Taiwan
[c] Department of Chemical and Materials Engineering, Chang Gung University, Taoyuan 33302, Taiwan. E-mail: kmlee@cgu.edu.tw
[d] College of Engineering, Ming Chi University of Technology, New Taipei City 24301, Taiwan

to improve narrowband OPDs include microcavity (MC) designs, charge collection narrowing (CCN), charge injection narrowing (CIN) and self-filtering (SF) structures.[5] For example, J. Yang *et al.* achieved an FWHM of 60 nm and an external quantum efficiency (EQE) of 18% using microcavity OPDs.[5c,6] B. Xie *et al.* demonstrated high responsivity with self-filtering narrowband OPDs, although this design is effective only for specific wavelengths and lacks versatility.[5e] Many researchers have explored the use of vapor deposition of organic and inorganic filters to create tricolor (Red/Green/Blue, RGB)-selective OPDs, which enhance the selectivity for narrowband wavelengths,[7] but this approach increases the production time and costs. Moreover, a key challenge for current narrowband OPDs is the need for thicker light-absorbing and depletion layers, which would reduce responsivity and detectivity of the OPDs. Therefore, there is still a lack of research related to highly efficient NIR OPDs for narrow-band detection.

Morphological optimization has been a widely used method to enhance the performance of OPDs, including techniques such as thermal annealing, solvent vapor annealing, and solvent additive addition. While thermal annealing and solvent vapor annealing can improve molecular alignment and crystallinity, these methods often require high temperatures and excessive solvents, which may not be suitable for large-scale manufacturing. In low-bandgap materials, the use of solvent additives such as 1,8-diiodooctane (DIO), 1-chloronaphthalene (CN), and 1,8-octanedithiol (ODT) can effectively control phase separation and molecular stacking of donor and acceptor materials.[8] However, the residual solvent additives can reduce the device stability because of photodegradation,[8c,9] requiring their removal through vacuum treatment, which complicates the process and limits mass production scalability. Recently, solid additives provided a simple and reliable method for morphology optimization. The solid additives can be divided into non-volatile solid additives such as 2-hydroxypyridine (2-DHP),[10] phosphorus quantum dots (PQDs),[11] and graphene-based porphyrin molecules (GO-TPP),[12] and volatile solid additives such as 1,4-diiodobenzene (DIB) and dithieno[3,2*b*:2′,3′-*d*]thiophene (DTT),[13] which can either remain within the active layer or volatilize from the active layer. The effects of these solid additives have been extensively discussed in organic photovoltaics (OPVs), where the solid additives were proven effective in increasing the molecular crystallinity and enhancing stability. However, no studies reported in the literature have yet explored the effect of solid additives on the response and dark current of the OPDs under reverse bias.

In this study, we used a solid additive, ferrocene (Fc), to improve the nanomorphology of the active layer consisting of PTB7-Th:BT-CIC, a well-known composition in OPVs for its high EQE at 830 nm.[14] Compared to conventional solvent additives such as CN and DIO, Fc can effectively inhibit the nanocrystal formation in the active layer, which improves charge transport and the performance of OPDs in the NIR region. Although perovskite materials have been widely explored for their tunable energy bandgap and high solution processability in optoelectronics,[15] their use as optical filters in OPDs has been less common. Here, we integrated perovskite films as optical filters for OPDs, leveraging their ability to precisely control the absorption range. This input optical filtering (IOF) allows us to achieve narrowband detection in the NIR region.[16] By tuning the thickness and absorption properties of the perovskite films, we obtained an EQE of 45% and a responsivity of 0.29 A W^{-1} at 820 nm under bottom illumination. Furthermore, we present a broadband–narrowband dual-mode NIR OPD, where the device can switch between broadband and narrowband detection modes, using a semi-transparent OPD. The dual-mode OPD allows for broadband detection (300–900 nm) with the highest EQE of 30% under top illumination. This integration of a low-cost perovskite filter and NIR OPDs demonstrated the capability of dual-mode OPDs for both narrowband and broadband detection. To the best of our knowledge, this work represents the first demonstration of a solid-state additive strategy applied to NIR OPDs, integrated with a perovskite-based optical filter and semi-transparent electrode to enable dual-mode detection. This multifunctional design uniquely combines morphological control, spectral selectivity, and dual-mode operation, offering a new platform for high-performance and application-flexible OPDs. Fig. 1(a–c) show the chemical

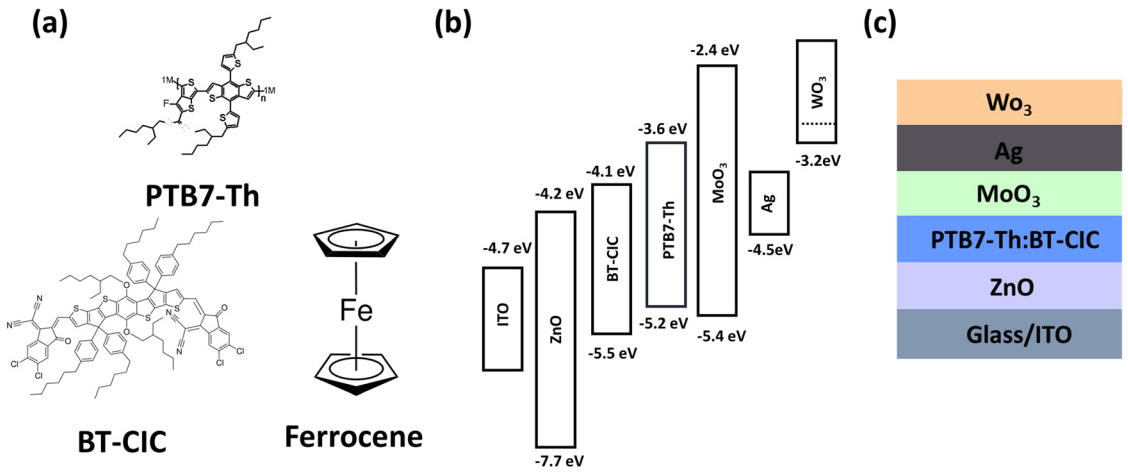

Fig. 1 (a) Chemical structures of donor PTB7-Th, acceptor BT-CIC and additive ferrocene. (b) Energy level diagram and (c) device architecture of OPDs.

structures of the active layer materials, the energy level diagram of the device, and the semitransparent OPD architecture with a modified electrode design.

2. Results and discussion

We first investigated the effect of various additives on the performance of OPDs in the NIR region, with a focus on optimizing the active layer thickness. Fig. S1(a) illustrates the relationship between the dark current density (J_d) and the active layer thickness in the absence of additives, showing that the thickness increased from 64 nm to 230 nm under a bias voltage of −1 V, and the J_d value decreased from 8.66×10^{-8} A cm^{-2} to approximately 8.65×10^{-9} A cm^{-2}. Although the OPD with a thicker active layer exhibited lower J_d, the FWHM of the responsivity increased by ~34 nm compared to the thinner active layer, making it less suitable for narrowband OPD applications (Fig. S1(b–d)). Therefore, we selected the device with 64 nm thickness, which exhibited the highest responsivity (0.47 A W^{-1}) at 820 nm for further optimization. Fig. S2–S4 illustrate the performance of devices with different concentrations of various additives. Fig. S2 illustrates the performance of devices with 0, 0.5, 1.5, and 3 vol% DIO. As the DIO concentration increased, both dark current and responsivity decreased, suggesting that DIO negatively impacts device performance. Fig. S3 shows that with the increase in CN concentration, the J_d value increased, while the responsivity decreased, with the optimal performance achieved at 1 vol% CN. Fig. S4 reveals the effect of ferrocene (Fc) at concentrations ranging from 1 to 12 wt% on device performance. As Fc concentration increased, the J_d value decreased and the EQE exhibited a red shift, with optimal performance at 6 wt% Fc. In Fig. 2a, we compared the J_d values under −1 V bias for devices optimized with the optimal concentrations of these additives. In these devices with a thickness of approximately 64 nm, the J_d value for the device without additives is 1.83×10^{-7} A cm^{-2}. For the CN (solvent additive) and Fc (solid additive), the J_d values were 1.47×10^{-8} A cm^{-2} and 6.81×10^{-9} A cm^{-2}, respectively. The J_d values were improved with the addition of various additives. Fig. 2b and c show the EQE and responsivity of these devices. At 830 nm, the EQE of the devices with Fc increased from 69.1% to 70.1%, and the responsivity increased from 0.446 A W^{-1} to 0.452 A W^{-1}. In contrast, both DIO and Fc additives reduce the responsivity to approximately 0.38 A W^{-1}. These results suggest that the different additives influence the internal structure and optoelectronic performance of the OPDs in distinct ways. Additionally, we compared the noise current and calculated the frequency range of 100 to 1000 Hz, the root-mean-square (rms) noise current ($I_{n,rms}$), to determine the specific detectivity (D^*_n) through the formulation (1).[17] Fig. 2d and e show that the OPDs with Fc additives achieved the lowest $I_{n,rms}$ of 3.32×10^{-14} A, resulting in a D^*_n value of 2.72×10^{12} Jones. We summarized the performances for OPDs with various additives in Table 1.

$$D^*_n = \frac{R\sqrt{A\Delta f}}{I_n} \quad (1)$$

To assess the impact of solid additive on device performance, we further investigated the effects of solvent and solid additives, CN and Fc, on the optical behaviors of the active layer in OPDs with similar performances. These optical results provide insights into how the two types of additives affect the molecular stacking and crystallinity of the active layer, thereby influencing charge generation and transport behaviors. Fig. S5a and b show the UV-Vis absorption spectra of the pure PTB7-Th

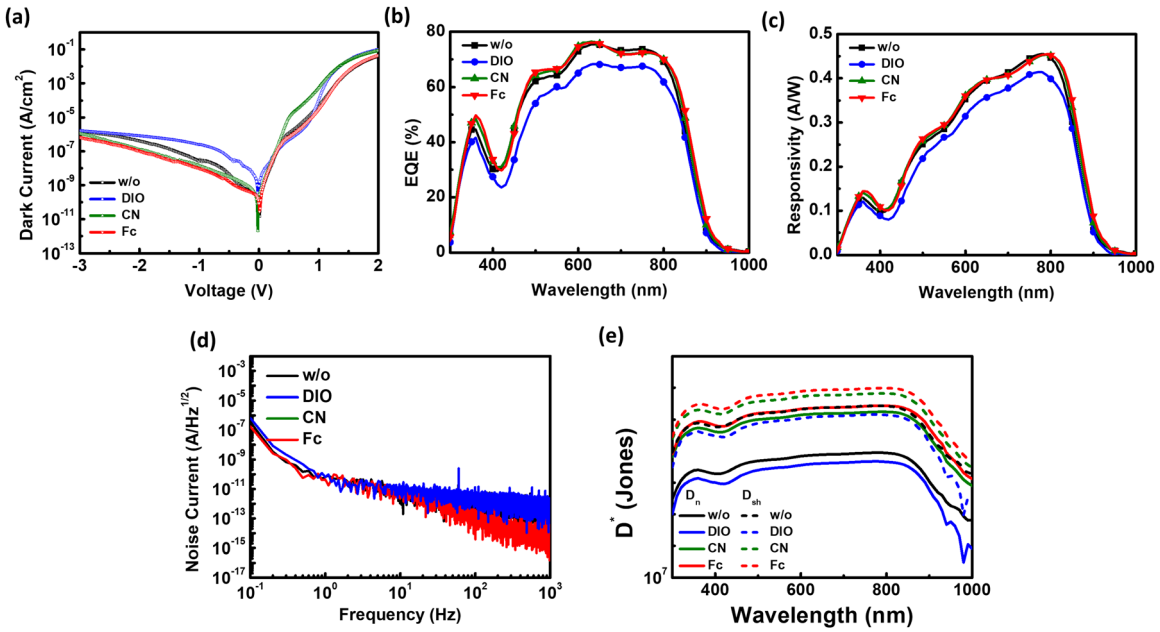

Fig. 2 Performance comparison of optimized devices with different additives: (a) dark current density under a −1 V bias for devices with and without additives, (b) external quantum efficiency, (c) responsivity, (d) noise current density, and (e) detectivity (D^*_n).

Table 1 Performance of organic photodetectors with different additives

Additive	EQE[ab] (%)	R^{ab} (A W^{-1})	Dark current density[b] (A cm^{-2})	$I_{n,rms}{}^{b}$ (A)	$D_n{}^{ab}$ (Jones)
w/o	69.1	0.446	8.66×10^{-8}	1.02×10^{-12}	8.75×10^{10}
DIO	61.8	0.398	5.91×10^{-7}	1.95×10^{-12}	4.56×10^{10}
CN	69.9	0.451	1.47×10^{-8}	5.15×10^{-14}	1.75×10^{12}
Fc	70.6	0.452	6.81×10^{-9}	3.32×10^{-14}	2.72×10^{12}

[a] Wavelength = 800 nm. [b] Under a −1 V bias for devices.

and BT-CIC films with CN and Fc. The main absorption ranges for PTB7-Th and BT-CIC are 300–750 nm and 600–900 nm, respectively. The complementary absorption behaviors of these two materials enable the blend of PTB7-Th:BT-CIC to cover the response range from visible to NIR wavelengths. After adding the CN additive, the absorption peak of pure PTB7-Th shifted by approximately 10 nm, from 750 nm to 760 nm, while the absorption peak of pure BT-CIC shifted by about 10 nm, from 830 nm to 820 nm. Previous studies have shown that CN improves the solubility of both donor and acceptor materials, affecting the crystallinity of the donor and acceptor materials.[8a] The red shift in the absorption peak of PTB7-Th indicates that the addition of CN enhanced the crystallinity of PTB7-Th, while the blue shift in the absorption peak of BT-CIC implies a decrease in crystallinity of BT-CIC. However, the absorption peaks of pure PTB7-Th and pure BT-CIC remained almost unchanged when Fc was added. Fig. S5(c) shows the absorption spectra of the blend of PTB7-Th:BT-CIC, where the main absorption region of BT-CIC remains obviously blue-shifted, due to a decrease in the crystallinity of BT-CIC in the blend film. These absorption results indicate that the incorporation of solid additive exhibits a minimal effect on the molecular ordering and crystallinity of the active layer.

To gain deeper insights into how these structural changes affect the morphology and molecular ordering within the blend films, we further analyzed their microstructural characteristics using grazing-incidence wide-angle X-ray scattering (GIWAXS) and atomic force microscopy (AFM). These measurements allowed us to compare the internal nanostructure and surface morphology of the active layer with CN and Fc. Fig. 3(a–c) present the 2-dimensional (2D) GIWAXS patterns for the active layer without and with the two additives, while the corresponding 1-dimensional (1D) profiles, including the in-plane (IP) and out-of-plane (OP) directions, are shown in Fig. S6. In the OP direction, the (010) peak positions of PTB7-Th and BT-CIC are located at 16.06 nm^{-1} and 17.70 nm^{-1}, respectively. For the blend films, the (010) peak positions of the films without any additive and with additives of CN and Fc, are observed at 17.22 nm^{-1}, 17.52 nm^{-1}, and 17.40 nm^{-1}, respectively. Using these peak positions, the corresponding π–π stacking distances were calculated to be 0.365 nm, 0.359 nm, and 0.361 nm, respectively. These values suggest that the CN additive leads

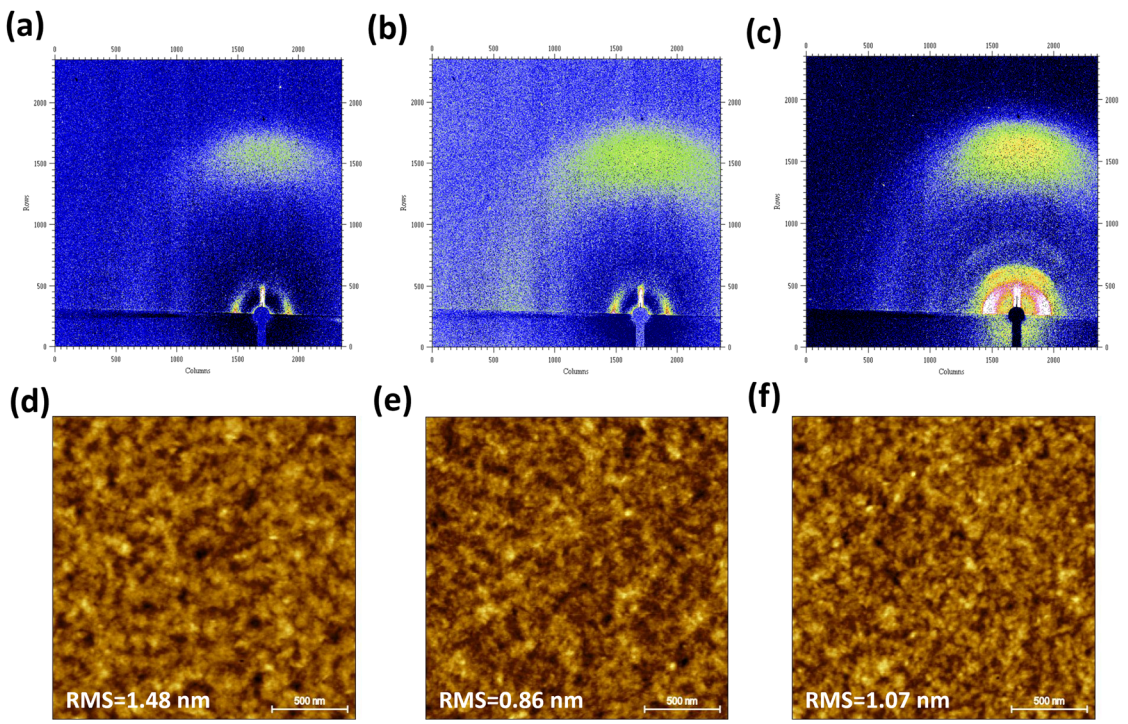

Fig. 3 Structural and morphological characterization of blend films with different additives. 2D GIWAXS patterns and AFM surface morphology images with root-mean-square (RMS) roughness of the films (a and d) without additive, (b and e) with CN and (c and f) with Fc.

to slightly tighter molecular packing in the active layer, while Fc appears to maintain similar packing compared to the film without additives. In the IP direction, the (100) peaks of PTB7-Th and BT-CIC are located at 2.69 nm^{-1} and 3.07 nm^{-1}, respectively, while in the blend films, the (100) peak positions for the pristine CB, CN additive, and ferrocene additive are 3.02 nm^{-1}, 3.17 nm^{-1}, and 3.07 nm^{-1}, respectively. These values correspond to the lamellar stacking distances, indicating that the films without additives and with CN result in smaller lamellar stacking distances. However, the Fc additive does not alter the stacking distance. The reduced lamellar stacking may disrupt the long-range order of molecular packing, weakening the diffraction intensity. As shown in Fig. S6(c), this is reflected in the broad and shallow diffraction peaks, suggesting that structural disorder may impact charge transport. Additionally, we measured the surface morphology (Fig. 3d–f) for the active layer without additive and with CN and Fc, yielding root-mean-square (RMS) roughness values of 1.48 nm, 0.86 nm, and 1.07 nm, respectively. These results indicate that the additives do not significantly alter the surface morphology of the active layers.

To further understand how the structural variations affect charge transport, we conducted EIS measurements to evaluate the effect of the two additives on the internal charge behavior of the active layer. A lower defect density reduces carrier recombination, enhancing the charge extraction efficiency, as illustrated in Fig. S7(a–c). The capacitance–frequency (C–F) and Nyquist impedance measurements revealed that the OPDs with Fc exhibited the lowest capacitance (1.3 nF) and the highest impedance (4.9×10^5 Ω). Additionally, the TPC results demonstrated that the carrier extraction time decreased from 0.77 μs to 0.64 μs with the Fc addition, which was attributed to the reduced trap density lowering the carrier recombination. Conversely, the carrier extraction time slightly increased to 0.79 μs for the OPDs with CN. Although CN also reduced the trap density, it improved the donor–acceptor (D–A) material compatibility and minimized phase separation between the D–A materials. While this suppressed dark current, it also increased the interfacial area between the donor and acceptor materials, thereby increasing the charge recombination efficiency during transport, which may ultimately slow carrier transport. We further evaluated the electron mobility of the OPDs with CN and Fc using the SCLC method,[18] as shown in Fig. S8(a–c). Upon adding Fc, the trap-filled-limited voltage (V_{TFL}) decreased from 1.52 V to 0.59 V, while the device with CN exhibited a V_{TFL} of 0.95 V. This reduction in V_{TFL} in the OPDs with Fc is attributed to improved molecular ordering, leading to a lower defect density. Furthermore, the electron mobility (μ) was calculated using eqn (2):

$$J = \frac{9}{8}\varepsilon_0\varepsilon_r\mu\frac{V^2}{L^3} \quad (2)$$

where ε_0 is the permittivity of free space, ε_r is the relative permittivity of the material, and L is the active layer thickness. The results indicate a significant increase in electron mobility upon the incorporation of Fc. In addition, the SCLC curves allow us to estimate the trap density (N_{trap}) using V_{TFL} *via* eqn (3):

$$N_{trap} = \frac{V_{TFL} \times 2_\varepsilon}{q \times L^2} \quad (3)$$

where V_{TFL} is the trap-filled-limited voltage, ε is the permittivity, q is the elementary charge, and L is the thickness of the active layer. Upon incorporating Fc, the trap density was found to decrease from 3.66×10^{16} cm^{-3} to 1.42×10^{16} cm^{-3}, indicating a substantial reduction in trap states. The corresponding electron mobility values are summarized in Table 2. To further elucidate the role of Fc, we systematically investigated a series of devices with different Fc concentrations (1.5–12 wt%) and extracted both trap densities and mobilities by the SCLC method. The results, presented in Fig. S8(d and e), reveal a concentration-dependent trend: electron mobility increases and trap density decreases with the increase in Fc content, reaching optimal values at 6 wt%. Notably, device responsivity also peaks at this concentration. These trends are conceptually summarized in Fig. S8(f), which illustrates the interrelationship between Fc concentration, trap density, charge transport, and photoresponse behavior. This correlation suggests that improved responsivity stems not only from enhanced charge transport but also from suppression of trap-assisted recombination. Additionally, we conducted high-sensitivity EQE and electroluminescence (EL) measurements in Fig. S9 and Table S1 to evaluate the non-radiative recombination and energy loss due to structural differences.[19] The energy loss (E_u) values for the OPDs without additive, and with CN and Fc were 39 eV, 41 eV and 38 eV, respectively. The EL-EQE values were 3.2×10^{-5}, 4.3×10^{-5} and 1.1×10^{-4}, respectively. The OPDs with Fc exhibited a lower E_u and a higher EL-EQE, confirming that Fc effectively improves structural ordering and morphology. This enhanced sub-bandgap response supports the interpretation that ferrocene facilitates a more favorable donor–acceptor interface, characterized by reduced trap-assisted recombination and improved charge extraction.

Table 2 SCLC, V_{TFL}, and trap density of OPDs without any additive, with CN and with Fc

Additive	Electronic mobility ($cm^2\ V^{-1}\ s^{-1}$)	V_{TFL} (V)	Trap density (cm^{-3})
w/o	9.08×10^{-5}	1.52	3.66×10^{16}
CN	2.14×10^{-4}	0.95	2.28×10^{16}
Fc	1.86×10^{-4}	0.59	1.42×10^{16}

We also measured the response speed and cutoff frequency of the devices. Fig. 4(a and b) present the rise time (τ_r) and fall time (τ_f) of the device response. For the OPDs without any additive, the τ_r and τ_f values were 478 ns and 455 ns, respectively. After incorporating Fc, the response speed significantly improved, with the τ_r and τ_f values reduced to 364 ns and 274 ns, respectively. In contrast, after adding CN, the τ_r and τ_f were 446 ns and 451 ns, respectively. This slow response time is due to the excessively fine phase separation within the active layer induced by CN, which increases the probability of carrier

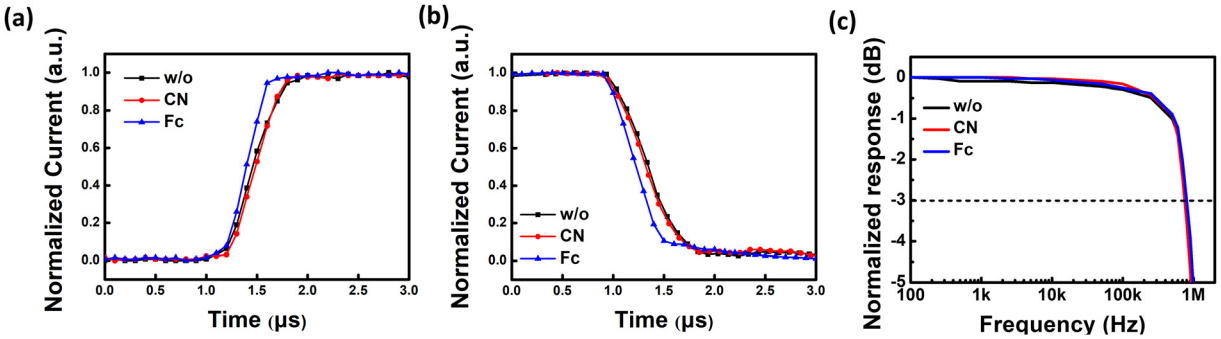

Fig. 4 Response speed and frequency characteristics of devices: (a) rise time (τ_r), (b) fall time (τ_f) and (c) cutoff frequency (f_{-3dB}) for OPDs without any additive, with CN and with Fc.

recombination during transport, hindering response speed. The cutoff frequencies (f_{-3dB}) of the OPDs with CN and Fc are improved due to the reduced trap density, increasing from 730 kHz to 754 kHz and 828 kHz, respectively, as shown in Fig. 4(c). To further demonstrate the generality of the solid additive strategy, we explored the incorporation of 6 wt% ferrocene into two additional high-performance donor–acceptor systems: PM6:BTP-eC9 and PTB7-Th:COTIC-4F. As shown in Fig. S10, the addition of ferrocene led to a moderate reduction in dark current in both systems, indicating suppressed charge injection under reverse bias. More notably, a consistent enhancement in EQE was observed, particularly in the wavelength range of 600–1000 nm. These findings confirm that the beneficial effects of ferrocene are not confined to a single material system, highlighting its potential as a broadly applicable solid-state additive for improving the photodetection characteristics of various OPD systems.

To realize broadband–narrowband dual-mode NIR OPDs, we demonstrated the integration of an optical filter and a transparent electrode, as illustrated in Fig. 5(a). We employed a thick perovskite film as a visible-light filtering layer for the PTB7-Th:BT-CIC system. Based on our previous studies, vacuum-deposited perovskite films exhibited excellent long-term operation stability under continuous illumination, with no observable degradation in dark current or photoresponse. Furthermore, no significant changes in optical absorption or crystallinity were detected over time, validating their suitability for optical sensing applications.[20] This stability makes vacuum-deposited perovskites a promising candidate for use as integrated optical filtering layers. We increased the perovskite film thickness to 1.7 μm, and the perovskite film exhibits a strong absorption in the 300–750 nm range, with high transmittance (~80%) beyond 750 nm, as shown in Fig. S11(a). This allows the OPDs

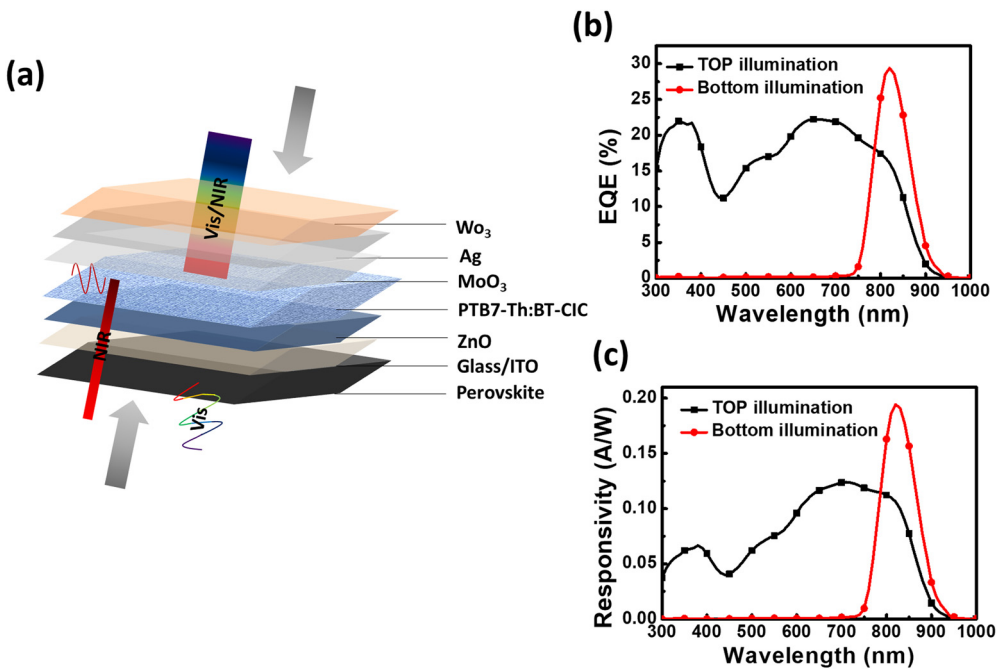

Fig. 5 (a) Schematic of the broadband–narrowband dual-mode NIR OPD integrating a perovskite optical filter and a transparent electrode. (b) EQE under top illumination with broadband light and bottom illumination with narrowband NIR light. (c) Responsivity comparison under different illumination conditions.

to maintain excellent responsivity in the NIR region, even after integrating the perovskite filter film (Fig. S11(b–d)). We deposited the perovskite filter onto the backside of the glass substrate of the OPDs to form integrated OPDs. We then compared the narrowband response of the integrated OPDs with the CN and Fc, as shown in Fig. S12. Compared to the CN additive, the OPDs with Fc exhibited an increase in EQE from 36.6% to 43.9% at 830 nm, and the responsivity increased from 0.245 A W^{-1} to 0.294 A W^{-1} (FWHM = 84.6 nm). These enhancements underscore the advantages of using solid-state additives such as ferrocene, which not only improved the photoresponse magnitude but also enhanced the spectral selectivity under narrowband operation. Based on our previous studies, we employed WO_3 surface modification to mitigate the high reflectivity of the silver electrode, thereby enhancing the performance of the semi-transparent electrode in organic photovoltaics.[21] This transparent electrode was then applied to this OPD system. Fig. S13(a) shows that reducing the Ag thickness from 100 nm to 12 nm had a minimal impact on the dark current, indicating that electrode thinning does not lead to excessive charge injection due to increased external electric fields. We further compared the performance of OPDs under top and bottom illumination. As illustrated in Fig. S13(b and c), when the OPDs with the Ag thickness from 100 nm to 12 nm are illuminated from the bottom, the EQE at 820 nm decreases from 70% to 54%, and the responsivity decreases from 0.465 A W^{-1} to 0.363 A W^{-1}. This is attributed to the increase in the sheet resistance caused by the Ag electrode thinning, thus hindering the charge transport. However, when the OPDs were illuminated from the top, the Ag electrode still caused light scattering even with the reducing Ag thickness of 10 nm, which limited the responsivity to approximately 0.1 A W^{-1}. To further evaluate the stability of the Ag/WO_3 semi-transparent electrode structure, we monitored the optical transmittance of the Ag/WO_3 bilayer under continuous 1 sun illumination for 7 days. As shown in Fig. S14(a), the transmittance spectra remained nearly unchanged, demonstrating excellent photostability of the electrode. Furthermore, the EQE spectra of Ag/WO_3-based OPDs stored in the dark for 7 days, presented in Fig. S14(b), exhibited no obvious degradation, confirming the long-term device operational stability of the Ag/WO_3-based OPDs.

Finally, we demonstrated the EQE and responsivity of the broadband–narrowband dual-mode OPDs under both bottom and top illumination, as shown in Fig. 5(b and c). The dual-mode OPDs achieved a broadband EQE (300–900 nm) of up to 20% under top illumination. In terms of responsivity, the dual-mode OPDs exhibited 0.12 A W^{-1} at 530 nm for the broadband response. For narrowband detection, the OPDs under bottom illumination exhibited an EQE of 29.4% and a responsivity of 0.19 A W^{-1} at 820 nm. We also demonstrated the actual response of the dual-mode OPDs under top illumination with green light (530 nm and 780 nm) and bottom illumination with NIR light (780 nm) (Fig. S15). We compared the performance of the state-of-the-art narrowband OPDs (Table S2) with that of the dual-mode OPDs (Table S3). Our research demonstrates a facile integration of low-cost perovskite filter and transparent electrode on the NIR OPDs with the potential for high-performance, broadband–narrowband detection.

3. Conclusion

In this study, the broadband–narrowband dual-mode NIR OPD system demonstrated substantial improvements in both visible and near-infrared detection performance through the optimization of material additives and device structure. The addition of Fc lowered the V_{TFL} value to 0.78 V, resulting in a reduced trap density of 2.60×10^{16} cm^{-3}, contributing to an improved charge transport and an enhanced device efficiency, along with the increase in EL-EQE to 1.1×10^{-4}%. The EQE at 800 nm increased from 69.1% to 70.1%, and the responsivity at this wavelength was boosted from 0.446 A W^{-1} to 0.452 A W^{-1}. The use of a perovskite filter enabled the OPDs to maintain a high EQE of 43.9% at 830 nm (FWHM = 84.6 nm). The use of a perovskite filter enabled the OPDs to maintain a high EQE of 43.9% at 830 nm (FWHM = 84.6 nm), while also achieving a broadband EQE of 30% (300–900 nm) in the dual-mode configuration under top illumination. The responsivity under top illumination was 0.17 A W^{-1}, and in dual-mode OPD narrowband under bottom illumination at 820 nm, it reached 0.29 A W^{-1}. This is the first work to validate the potential application of solid additives in OPDs and highlight the critical role of material and structure optimization in improving the performance of dual-mode OPDs. It paves the way for their application in advanced optoelectronic devices with enhanced responsivity across different spectral regions.

4. Experimental section

4.1. Materials

PTB7-Th and BT-CIC were purchased from 1-Material Inc., while zinc acetate was obtained from Alfa Aesar. Other chemicals including 2-methoxyethanol, ethanolamine, chlorobenzene (CB), ferrocene (Fc), 1,8-diiodooctane (DIO), 1-chloronaphthalene (CN), and molybdenum trioxide (MoO_3) were sourced from Sigma-Aldrich. All chemicals and solvents were used as received without further purification.

4.2. Device fabrication

OPDs were fabricated on indium tin oxide (ITO)/glass substrates. The substrates were cleaned sequentially with deionized water, acetone, and isopropanol using an ultrasonic bath, with each step lasting 30 minutes. ZnO was deposited as the electron transport layer (ETL) onto the cleaned ITO substrates, followed by annealing at 170 °C for 30 minutes. ZnO was synthesized *via* a sol–gel method according to a previously reported procedure.[22] Afterward, the substrates were transferred into a nitrogen-filled glovebox. PTB7-Th and BT-CIC were used as donor and acceptor materials, respectively. They were dissolved in CB at a weight ratio of 1/1.5, with a total concentration of 20 mg mL^{-1}. Various additives were introduced, including DIO, CN, and Fc. In the DIO system, DIO was

added at concentrations of 0.5 vol%, 1.5 vol%, and 3 vol%, while in the CN system, CN was introduced at concentrations of 1 vol%, 3 vol%, and 5 vol%. In the Fc system, Fc was incorporated into the active layer solutions at concentrations of 3 vol%, 6 vol%, 9 vol%, and 12 wt%. The prepared active layer solution was spin-coated onto glass/ITO/ZnO substrates for 30 seconds, yielding an active layer thickness of approximately 100 nm. These solutions were stirred at 65 °C in the glovebox for 12 hours before spin-coating. Subsequently, MoO_3 (5 nm, hole transport layer, HTL) and Ag (100 nm) were deposited onto the active layer *via* thermal evaporation. The device area was 0.04 cm^2. For the design of the dual-mode OPD, we reduced the upper Ag layer to 12 nm and deposited 30 nm of WO_3 to lower the surface reflectivity of the Ag. The chemical composition of the perovskite layer as an optical filter used in this experiment was based on the previous study.[20] Perovskite films were deposited using a thermal evaporation system under a base pressure of $\sim 2 \times 10^{-6}$ Torr. The deposition rates were maintained at 0.5–1.0 Å s^{-1} for all materials, except for silver, which was deposited at 3.0 Å s^{-1}. For the perovskite layer, CsBr, formamidinium iodide (FAI), and PbI_2 were co-evaporated at rates of 0.6, 0.9, and 0.6 Å s^{-1}, respectively. The FAI source was maintained at 190–195 °C, while the substrate was actively cooled to 8 °C to promote uniform film formation. The thicknesses of the individual layers were monitored in real time using a quartz crystal microbalance (QCM). Following deposition, the films and completed devices were annealed at 135 °C for 30 minutes on a hot plate to promote crystallization.

4.3. Characterization

The current density–voltage (*J–V*) characteristics under dark conditions were measured using a programmable source meter (Keithley 2636A) in the sweep measurement mode. The EQE spectrum and responsivity, covering the 300–1000 nm range, were recorded in the DC mode using a QE-R system (Enlitech, Taiwan), calibrated using a Si-based photodetector (Hamamatsu S1337) to ensure accurate monochromatic light detection. For evaluating the frequency response and linear dynamics range of OPDs, a commercial LED (Thorlabs) with emission wavelengths of 780 nm and 530 nm was used. The LED was tuned to a flux density of 1 mW cm^{-2} and connected to a function generator (Tektronix AFG3102C), which generated pulses to trigger the OPDs. The absorption characteristics of the samples were measured using a UV-visible spectrometer (Jasco V-750), and the wavelength half-width was calculated. Electrochemical impedance spectroscopy (EIS) was conducted using a Solartron Materials Lab XM system, scanning in the frequency range of 10^{-1} to 1 MHz with a sinusoidal AC signal of 1 V amplitude. The defect density and charge mobility of the devices were determined *via* space-charge-limited current (SCLC) measurements. The carrier extraction time and recombination rates were analyzed by the EIS and transient photocurrent (TPC) measurements using a Fluxim Paios characterization suite. Surface morphology and roughness of the thin films were examined by atomic force microscopy (AFM, Bruker). Energy loss characteristics were further evaluated using a Fourier-transform photocurrent spectroscopy external quantum efficiency (FTPS-EQE) spectrum (Enlitech).

Author contributions

Yu-Ching Huang: writing – original draft, supervision, conceptualization. Zhi-Hao Huang: writing – original draft, formal analysis, data curation. Bo-Chen Chen: formal analysis, data curation Hou-Chin Cha: writing – review & editing, Kun-Mu Lee: writing – review & editing.

Conflicts of interest

The authors declare no conflict of interest.

Data availability

The data supporting this article have been included as part of the SI.

Supplementary information available: Detailed device performance comparisons for various additive-based devices, GIWAXS measurements, multiplecomponent blend film characteristics, stability tests, electrical characterization, carrier mobility evaluation, and trap density analysis. See DOI: **https://doi.org/10.1039/d5tc02658j**

Acknowledgements

This research was supported in full by the National Science and Technology Council of Taiwan (Grant numbers: NSTC 112-2622-E-131-011, NSTC 112-2628-E-131-001-MY4, NSTC 114-2222-E-131-002, 114-2221-E-131-012-MY3, 111-2223-E-182-001-MY4), Chang Gung University (URRPD2Q0041), and Chang Gung Memorial Hospital, Linkou, Taiwan (CMRPD2P0091).

References

1 (*a*) J. Müller, *Advances in Electronics and Electron Physics*, ed. L. Marton, C. Marton, Academic Press, 1981, vol. 55, p. 189; (*b*) D. Friedrich, W. John, O. Krüger, S. Nowy, D. Prasai, P. Sperfeld, G. Wagner, T. Weiss, L. Weixelbaum and S. Winter, *J. Mater. Res.*, 2013, **28**, 33; (*c*) T. Shan, X. Hou, X. Yin and X. Guo, *Front. Optoelectron.*, 2022, **15**, 49; (*d*) G. Simone, M. J. Dyson, S. C. J. Meskers, R. A. J. Janssen and G. H. Gelinck, *Adv. Funct. Mater.*, 2020, **30**, 1904205.

2 (*a*) Q. Li, Y. Guo and Y. Liu, *Chem. Mater.*, 2019, **31**, 6359; (*b*) Z. Wang, S. Cheng, K. Fukuda, W. Hu, X. Xu and T. Someya, *Wearable Electron.*, 2024, **1**, 53.

3 Z. Li, Z. He, C. Xi, F. Zhang, L. Huang, Y. Yu, H. H. Tan, C. Jagadish and L. Fu, *Adv. Mater. Technol.*, 2023, **8**, 2202126.

4 A. Armin, R. D. Jansen-van Vuuren, N. Kopidakis, P. L. Burn and P. Meredith, *Nat. Commun.*, 2015, **6**, 6343.

5 (*a*) K.-W. Tsai, G. Madhaiyan, L.-H. Lai, Y.-T. Hsiao, J.-L. Wu, C.-Y. Liao, C.-H. Hou, J.-J. Shyue and Y.-M. Chang, *ACS Appl.*

Mater. Interfaces, 2022, **14**, 38004; (*b*) M. Liu, J. Wang, Z. Zhao, K. Yang, P. Durand, F. Ceugniet, G. Ulrich, L. Niu, Y. Ma, N. Leclerc, X. Ma, L. Shen and F. Zhang, *J. Phys. Chem. Lett.*, 2021, **12**, 2937; (*c*) J. Yang, J. Huang, R. Li, H. Li, B. Sun, Q. Lin, M. Wang, Z. Ma, K. Vandewal and Z. Tang, *Chem. Mater.*, 2021, **33**, 5147; (*d*) Z. Lan, Y. S. Lau, Y. Wang, Z. Xiao, L. Ding, D. Luo and F. Zhu, *Adv. Opt. Mater.*, 2020, **8**, 2001388; (*e*) B. Xie, R. Xie, K. Zhang, Q. Yin, Z. Hu, G. Yu, F. Huang and Y. Cao, *Nat. Commun.*, 2020, **11**, 2871; (*f*) S. Xing, X. Wang, E. Guo, H. Kleemann and K. Leo, *ACS Appl. Mater. Interfaces*, 2020, **12**, 13061; (*g*) Y. Zhao, N. Chen, B. Deng, L. Wu, S. Wang, B. Grandidier, J. Proust, J. Plain and T. Xu, *ACS Appl. Mater. Interfaces*, 2023, **15**, 49436.

6 Y. Wang, J. Kublitski, S. Xing, F. Dollinger, D. Spoltore, J. Benduhn and K. Leo, *Mater. Horiz.*, 2022, **9**, 220.

7 (*a*) D. Kim, H.-J. Park, S.-H. Jung, W. J. Pyo, S. Z. Hassan, H. R. Sim, J.-H. Lee, D.-W. Jee and D. S. Chung, *Adv. Mater.*, 2024, **36**, 2309416; (*b*) S. Yoon, K. M. Sim and D. S. Chung, *J. Mater. Chem. C*, 2018, **6**, 13084.

8 (*a*) E. Moustafa, A. A. A. Torimtubun, J. Pallarès and L. F. Marsal, *Sol. RRL*, 2022, **6**, 2100480; (*b*) C. Montenegro Benavides, S. Rechberger, E. Spiecker, M. Berlinghof, T. Unruh, M. Biele, O. Schmidt, C. J. Brabec and S. F. Tedde, *Org. Electron.*, 2018, **54**, 21; (*c*) H. Waters, N. Bristow, O. Moudam, S.-W. Chang, C.-J. Su, W.-R. Wu, U. S. Jeng, M. Horie and J. Kettle, *Org. Electron.*, 2014, **15**, 2433.

9 A. Tournebize, A. Rivaton, H. Peisert and T. Chassé, *J. Phys. Chem. C*, 2015, **119**, 9142.

10 B. Xu, G. Sai-Anand, G. E. Unni, H.-M. Jeong, J.-S. Kim, S.-W. Kim, J.-B. Kwon, J.-H. Bae and S.-W. Kang, *Appl. Surf. Sci.*, 2019, **484**, 825.

11 R. Gui, H. Jin, Z. Wang and J. Li, *Chem. Soc. Rev.*, 2018, **47**, 6795.

12 Y.-F. Ma, Y. Zhang and H.-L. Zhang, *J. Mater. Chem. C*, 2022, **10**, 2364.

13 S. Bao, H. Yang, H. Fan, J. Zhang, Z. Wei, C. Cui and Y. Li, *Adv. Mater.*, 2021, **33**, 2105301.

14 Y. Li, J.-D. Lin, X. Liu, Y. Qu, F.-P. Wu, F. Liu, Z.-Q. Jiang and S. R. Forrest, *Adv. Mater.*, 2018, **30**, 1804416.

15 (*a*) C.-Y. Chang, Y.-L. Chin, C.-Y. Chang and J. Holovský, *Adv. Funct. Mater.*, 2025, 2422732; (*b*) J. Y. Kim, J.-W. Lee, H. S. Jung, H. Shin and N.-G. Park, *Chem. Rev.*, 2020, **120**, 7867.

16 H. Liang, J. Zhang, X. Zhao, Y. Ye, X. Liu, L. Li, G. Yang and J. Huang, *Small*, 2025, 2501140.

17 (*a*) Z. Wu, N. Li, N. Eedugurala, J. D. Azoulay, D.-S. Leem and T. N. Ng, *npj Flexible Electron.*, 2020, 4; (*b*) C. Fuentes-Hernandez, W.-F. Chou, T. M. Khan, L. Diniz, J. Lukens, F. A. Larrain, V. A. Rodriguez-Toro and B. Kippelen, *Science*, 2020, **370**, 698.

18 V. M. Le Corre, E. A. Duijnstee, O. El Tambouli, J. M. Ball, H. J. Snaith, J. Lim and L. J. A. Koster, *ACS Energy Lett.*, 2021, **6**, 1087.

19 Q. Liu and K. Vandewal, *Adv. Mater.*, 2023, **35**, 2302452.

20 N. R. Al Amin, C.-C. Lee, Y.-C. Huang, C.-J. Shih, R. Estrada, S. Biring, M.-H. Kuo, C.-F. Li, Y.-C. Huang and S.-W. Liu, *ACS Appl. Mater. Interfaces*, 2023, **15**, 21284.

21 Y.-C. Huang, C.-C. Lee, Y.-Y. Lee, S.-Y. Chung, H.-C. Lin, U. Kasimayan, C.-F. Li and S.-W. Liu, *Mater. Adv.*, 2024, **5**, 2411.

22 Y.-M. Sung, A. K. Akbar, S. Biring, C.-F. Li, Y.-C. Huang and S.-W. Liu, *J. Mater. Chem. C*, 2021, **9**, 1196.